Precursory flow in the formation of cellulose nanofiber films revealed by multiscale image analysis

Haruto Watanabe and Itsuo Hanasaki [*]

Institute of Engineering, Tokyo University of Agriculture and Technology, Naka-cho 2-24-16, Koganei, Tokyo 184-8588, Japan

Film materials made of cellulose nanofibers (CNFs), i.e., so-called nanopapers, are fabricated from aqueous dispersions of CNFs. The drying in the container causes the phase transition from sol to gel and final state of transparent film. The nonequilibrium and nonuniform nature of the drying calls for the least invasive in-process measurement to understand the process. In this paper, we focus on the transient state of nanopaper formation through the time-series image analysis from optical measurements on the multiple spatiotemporal scales and resolutions. The combination of single-particle tracking and particle image velocimetry reveals the intermittent flow with a low symmetry of space pattern in the middle stage of drying process. The small portion of CNF is sufficient for suppression of coffee-ring phenomena, and the flow is in combination with the emergence of partial structural order. Furthermore, we find that the flow pattern depends on the sidewall material of the sample container. We characterize the three stages of drying process through the flow patterns by the correlation length of velocity autocorrelation function as well as the mean and standard deviation of the flow speed in the containers.

I. INTRODUCTION

Cellulose nanopapers [1–4] are one of the promising materials that covers the vast range of application in terms of printed electronics [5], green electronics [6], flexible device [2], etc. The nanopaper is similar in its chemical elements to cellulose, but substantial difference originates from the fibrous elements, the cellulose nanofibers (CNFs) [7]. Namely, the fine texture of CNFs provides the suitability for printed electronics [5] and transparency [8] in contrast to the conventional papers. Device applications are compared with those based on silicon-based substrates. The obvious advantage of nanopapers is flexibility, which is founded on the basic mechanical properties [9–18]. The mechanical properties depend on their microscopic collective structure as well as the CNF as the element. Surface topography and texture of bare nanopapers are important in the printed electronics [19] and transparency [8,20]. Furthermore, recent active pursuit of surface modification to control hydrophilic/hydrophobic characteristics [21–24] increases the importance of surface properties in view of applications in microfluidic paper-based analytical devices [25,26].

When the same CNFs are employed, structural characteristics of the nanopaper is determined when drying the aqueous dispersion of CNFs [20,27–30]. Sufficiently dilute CNF dispersion is a kind of sol [31–34] where CNFs diffuse in the dispersant water. Drying of CNF dispersion causes the increase in CNF concentration, leading to the gel state. The drying from the gel state finally provides the nanopaper structure. The transition of the physical state from the sol with low viscosity to the structured state of CNFs is useful for the prevention of coffee-ring effect in the sessile droplet [35,36], which is, in turn, direct relevance to the printed electronics. When gelation takes place in the CNF dispersion during the drying process, this random network formation is not as clear as the typical crystallization phenomena. The unclear boundary between the sol and the gel state is also recently revealed from universal point of view [37]. In fact, even crystal nucleation of the organic molecule in solution includes the physical state between the liquid and the solid [38]. The rheological measurements could be the means to know the structural order between the complete sol and the gel. However, the conventional approach based on the shear flow cannot reveal the delicate process of structural formation by definition as it destroys the incomplete structural order. The discussion based on those rheometers should be consistent with the principle and the available information [31,32].

In contrast, the microrheological approach based on the single-particle tracking (SPT) [33] is much less invasive, and it is a suitable platform to understand the structural formation of nanopapers from aqueous CNF dispersion. Brownian dynamics of probe particles in the dispersion contains rich information of the surrounding environment, i.e., the rheological state of the dispersion. Although the Stokes-Einstein relation is useful for deriving viscosity from the diffusion coefficient, the framework of the generalized diffusion coefficient [39] tells more than viscosity but the existence of structural order through the subdiffusive behaviors [33]. In contrast to the microparticle image velocimetry (μPIV), the Brownian trajectories provides rheological information in equilibrium without flow [34]. The fact that there is a transient state between the complete sol and the gel may had been

*[*]hanasaki@cc.tuat.ac.jp

supposed without clear experimental evidence. However, it has been recently clarified by the microscopy movie data analysis [34] based on SPT empowered by the simple theoretical methodology of logarithmic measure [40] that reveals the multimodal diffusion.

The drying process of nanopaper fabrication involves the basic space nonuniformity in the physical condition. The sol or liquid samples need to be placed in containers, and the evaporation of dispersant water takes place only from the air-liquid interface. Then, the progress of drying can be nonuniform in the container. The drying process accompanies the hydrogen bonding between the CNFs, which causes residual tensile stress of the fabricated sheet structures [41]. In our previous study [30], we observed the slight yet significant rise of the generalized diffusion coefficient and its scaling exponent before their drastic decrease toward the completion of drying up. It can be the hallmark of localized temporary flow caused by the tensile force by precedent hydrogen-bond network of the subdomain in the whole system. The above-mentioned partial structural order at a certain range of CNF concentration [34] is consistent with this hypothetical interpretation. If the tensile force breaks the symmetry of the system at the scale of the container, it works as the possible origin of nonuniformity in the nanopaper. In the case of least initial concentration of CNFs to suppress the coffee-ring effect of sessile colloidal droplet, the nonuniformity of dispersed material distribution was not observed from the overall picture of the dried films [35,36]. Therefore, the basic characteristics of nonequilibrium drying process that connects the CNF dispersion and nanopaper need to be clarified.

In this paper, we focus on the transient phenomena between the sol and the gel states of aqueous CNF dispersion. High spatiotemporal resolution of the SPT-based microrheological analysis is advantageous for the understanding of possible nonuniformity in space and time, in contrast to the conventional rheometer that assumes the homogeneity of samples. Since the high resolution of the data directly means the huge data storage amount, we reach the longer temporal scale by repeating the movie capture with time intervals and the larger space scale by changing the location of this interval movie capturing. However, the data obtained from this approach have a limitation that it is not synchronized at the full scale. Although it can cover the characteristics with full reproducibility including time, the transient events with randomness in the time point is only partly determined. Therefore, we also resort to the μPIV with lower resolution than the SPT to combine with it. It covers the stochastic nonuniformity of the system at the container scale of a drying sample. We show that there is a spatiotemporal nonuniformity in the structural formation process of nanopapers. In particular, transient flow occurs within the certain time and space ranges in a stochastic manner. This is a significant step forward to understand what takes place in the drying process of CNF dispersion to form nanopapers.

II. METHODS

A. Sample preparation

1. Aqueous dispersion of CNFs with probe particles

The sample liquid consists of CNFs, probe particles, and water. The probe particles are used for the SPT, but the same particle dispersion is also useful for the PIV. We use TEMPO-oxidized CNFs (I-2SX, DKS Co. Ltd.), and polystyrene particles with a diameter of 1.4 μm (Chemisnow, SX-130H, Soken Chemical & Engineering, Co., Ltd.). The concentration is tuned by dilution using purified water (Purified water, KENEI Pharmaceutical Co., Ltd.). The dilution and mixing proceeds as follows. The aqueous CNF dispersion with a concentration of 0.44 wt% without particles was prepared from 2.2 wt% CNF. The particle dispersion without CNFs was prepared with a concentration of 1.0 wt%. We measured the mass of the viscous CNF dispersion sample with electronic balance (MS205DU, Mettler-Toledo, LLC) to cope with the error of pipetting quantity due to the viscosity. Then, CNF dispersion and particle dispersion was mixed and further diluted to prepare the aqueous CNF/particle dispersion with 0.1 wt% of CNF and 0.05 wt% of particles.

The mixing and/or dilution is based on the motion of vial container (1392-150-SS-LP-CS, FUKAEKASEI Co., Ltd and WATSON Co., Ltd.) with a mixer (AR-100, THINKY CORPORATION) after hand vibration of the sealed vial. The mixing motion consists of rotation (spinning) at 800 revolutions per minute (rpm) in combination with revolution at 2000 rpm for 2 min. After the mixing motion of 2 min., degassing motion of revolution at 2200 rpm for 2 min without rotation was conducted. Finally, an ultrasonic homogenizer (NR-50M-MT2, Microtec Co., Ltd.) was used at 30% of the power of the pulse width modulation mode for 30 s.

2. Containers to dry the samples

We prepared two types of sample container used in the measurements as shown in Fig. 1. The difference between the two containers is the sidewall material. Although only the container with the PTFE sidewall is used in the measurements for the SPT, that with the silicone sidewall is also used in the measurements for PIV. PTFE exhibits relatively low wettability against water. Silicone is well known for the sealing functionality against glass to adhere without additional material. We expected the difference of sidewall wettability can affect the
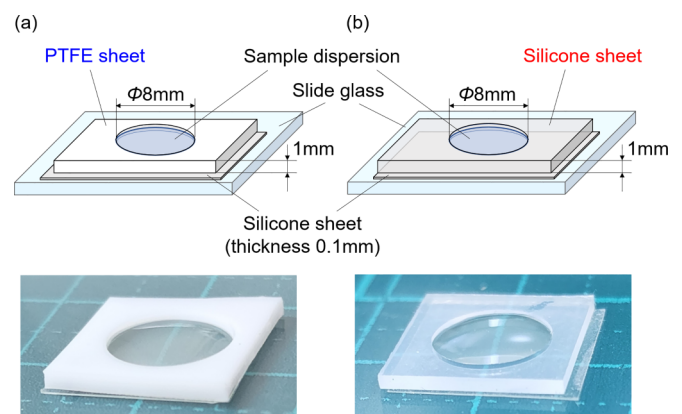

FIG. 1. Schematics and digital camera images of the sample containers with sidewalls of 1-mm height consisting of (a) polytetrafluoroethylene (PTFE) and (b) silicone, respectively. It should also be noted that the sidewall with a height of 0.1 mm from the bottom consists of a silicone sheet in both cases of (a) and (b) so that the sealing of bottom gap is satisfied.
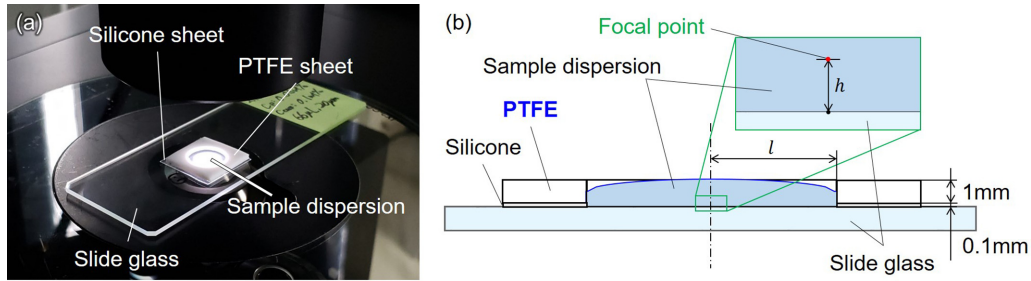
FIG. 2. Sample set up for SPT obtained by inverted optical microscope. The sidewall of the cylindrical container with a diameter of 8 mm consists of PTFE sheets. $l = 4$ mm corresponds to the horizontal center in the container, whereas $l < 4$ mm indicates the distance closer to the sidewall whereas keeping the same container diameter 8 mm.

overall dynamics of the sample drying process. The container shape has a diameter of 8 mm with a height of 1.1 mm. The bottom wall consists of slide glass (S9915, Matsunami Glass Ind., Ltd.), and the bottom part of the sidewall with a height of 0.1 mm consists of silicone sheet (6-9085-12, AS ONE Corporation) to seal the gap between the glass of bottom wall and the PTFE of sidewall. A 1-mm height of the sidewall consists of a PTFE sheet (9000-S, NICHIAS Corporation) for one of the two types of sample containers. We simply call the container configuration shown in Fig. 1(a) as the container with the PTFE sidewall hereafter in this article. On the other hand, we call the container configuration shown in Fig. 1(b) as the container with the silicone sidewall where the top 1 mm of the sidewall consists of silicone sheet (SR-50, TIGERS POLYMER CORPORATION). The sample liquid with a mass of ca. 63 mg was placed in the container with a volume of 55 μL, thereby the initial macroscopic shape of the sample liquid is convex upward (cf. Figs. 1 and 2).

B. Measurement

1. Optical microscopy movie

We captured the movie of optical microscopy to the sample as shown in Fig. 2 for the SPT analysis. A scientific complementary metal-oxide–semiconductor camera (Zyla5.5, Andor Technology Ltd.) was mounted on an inverted optical microscope (IX73, Olympus Corporation) with a phase contrast setup. The objective lens was 20× and the pixel pitch of the camera was 6.5 μm. The frame interval of the movie capture was 10^{-2} s with an exposure time of 9×10^{-4} s. A single frame of the image consists of 512×512 px^2 corresponding to 166.4×166.4 μm^2. A single movie consists of 10^3 frames corresponding to 10 s. The movie data were obtained with an interval of 5 min. The first movie was captured 10 min after the sample liquid pipetting. The end of movie capture was decided by the visual inspection of drying up. The room temperature was 20–30 °C and the humidity was 30–40% relative humidity. The height measurement was based on the dial of the inverted microscope. The refractive index 1.33 was multiplied to the nominal value of the dial increments to transform the nominal values to the actual values in water.

2. Digital camera images in time series

We obtained time-series images of the whole range of sample bottom wall area by the digital camera (DMC-GX8,

Panasonic Corporation) with a macrolens (M.ZUIKO DIGITAL ED60-mm F2.8 Macro, Olympus Corporation). The images were captured from the vertical top position without magnification. The light source was white LED light (AS-1002, FUJIFILM Corporation). The camera, sample, and light source are surrounded by the white studio box (DSB-75, HAKUBA Photo Industry Co., Ltd.), where the original open plane was also covered with a backscreen.

The sidewall of the container can affect the sample dynamics through the microscopic surface property and macroscopic boundary shape. The opaque or insufficiently transparent
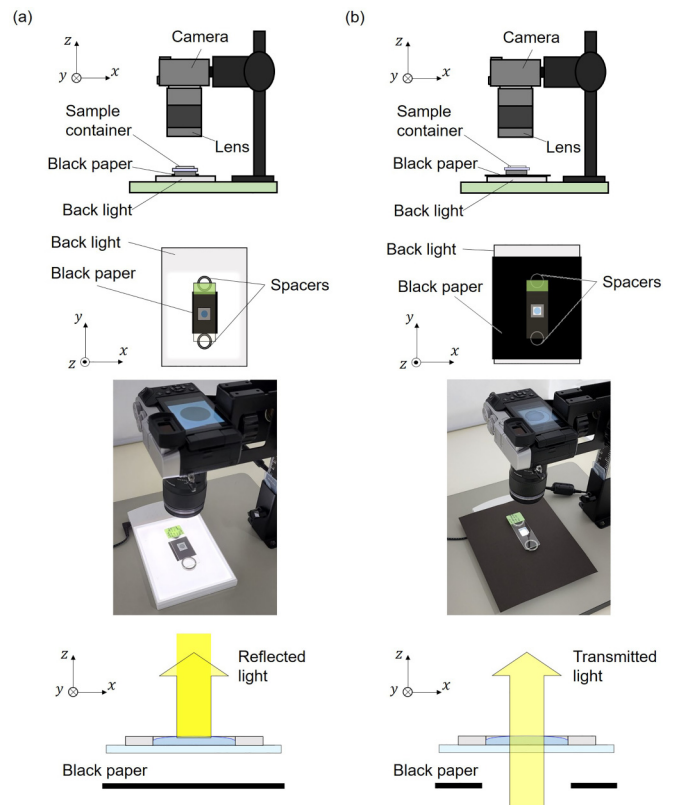

FIG. 3. Illumination and camera configurations employed to obtain the time-series images for PIV analysis with (a) indirect and (b) direct illumination. The reflected light from the sample surface is mainly captured by the camera in the indirect illumination, whereas the white light-emitting diode (LED) light directly transmits through the sample to reach the camera in the direct illumination.
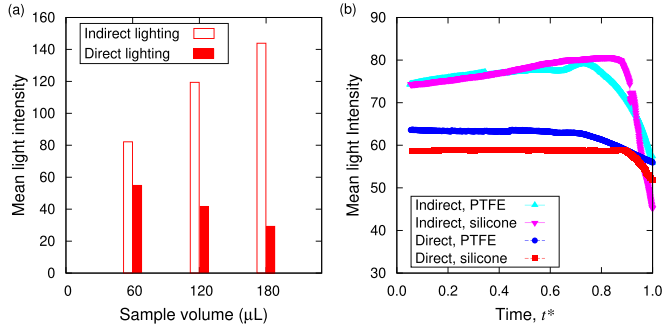
FIG. 4. The difference between indirect and direct lighting setups in terms of light intensity characteristics as a function of (a) sample volume and (b) drying time series. The light intensity is evaluated by the mean value among pixels in the sample domain. The absolute value of light intensity depends on the camera setups, which are different for indirect and direct lightings (cf. Sec. II B 2). The difference of sample volume approximately corresponds to the sample thickness due to the same container bottom area with the silicone side wall. The sidewall height (i.e., the thickness of a silicone sheet) for (a) was 5 mm to accommodate the increased sample volume.

walls do not allow the direct precise positioning of vertical position in the macroscopic measurement. Therefore, we examine the typical two types of illumination configuration. Figure 3(a) shows the indirect illumination where the light from the LED mainly reaches the sample from the upper side and the reflected light reaches the camera. Figure 3(b) shows the direct illumination where the light from the LED mainly transmits through the sample vertically to reach the camera.

The camera settings for indirect illumination are F-value 8, shutter speed 0.2 s, and ISO sensitivity 800, whereas those for direct illumination are F-value 8, shutter speed 10^{-2} s and ISO sensitivity 200. Indirect illumination through reflected light mainly contains the signal in the vicinity to the surface. This is an advantage when the flow field substantially depends on the vertical position. Direct illumination through transmitted light includes the whole depth signal from the sample. This is an advantage when the flow direction does not substantially depend on the vertical position. The camera capture started from 10 min after the placement of the liquid samples to the containers, and the frame interval was 10 s. The possible depthwise dependence is analyzed through the SPT instead of the PIV.

The difference of the above-mentioned lighting setup is examined by preliminary experiments as shown in Fig. 4. The direct lighting shows decrease in light intensity with increasing sample thickness due to the decrease in light transmission [Fig. 4(a)]. In contrast, the light intensity signal increases for indirect lighting with increasing sample thickness since the signal originates from the reflected light. The increase in signal intensity with thickness rather than constant signal intensity is partly attributed to the relative configuration of the air-liquid interface against the sidewall. The increase in sample concentration by the drying process to the middle stage with constant total amount of dispersed materials leads to the increase in the light intensity signal for indirect lighting in contrast to the constant light intensity for direct lighting [Fig. 4(b)].

TABLE I. Input parameters for the SPT by the algorithm of Sbalzarini and Koumoutsakos [42].

Parameter	Value
Particle radius (px)	4
Intensity percentile (%)	0.1
Cutoff score (−)	0
Displacement threshold (px)	2
Link range (frames)	1

C. Data analysis

1. SPT and evaluation of generalized diffusion

The trajectories of probe particles were obtained by the algorithm of Sbalzarini and Koumoutsakos [42] using the input parameters shown in Table I. The physical states of samples were evaluated by the framework of generalized diffusion [39,45]. Since frame interval of the camera was sufficiently long compared to the inertial time correlation of the particle dynamics, the time evolution of mean-squared displacements are described as

$$2n_{\mathrm{d}}D_{\alpha}t^{\alpha} \simeq \langle |\boldsymbol{r}(t) - \boldsymbol{r}(0)|^2 \rangle, \qquad (1)$$

where $\langle \cdot \rangle$ indicates the ensemble average, n_{d} is the dimension of position vector $\boldsymbol{r}$, and t is the time. D_{α} and α are the generalized diffusion coefficients and their scaling exponent, respectively. $\alpha = 1$ corresponds to the normal diffusion, and $\alpha < 1$ indicates the subdiffusive behavior. In the numerical evaluation of trajectories obtained from the SPT, the following equation is used [30,33,34,36]:

$$\frac{\sum_{i=1}^{N_{\mathrm{I}}} \sum_{j=1}^{N_{Fi}-1} |\boldsymbol{r}_i(t_{j+1}) - \boldsymbol{r}_i(t_j)|^2}{2n_{\mathrm{d}} \sum_{i=1}^{N_{\mathrm{I}}} (N_{Fi} - 1)} \simeq D_{\mathrm{FB}\alpha} \Delta t_{\mathrm{frm}}^{\alpha_{\mathrm{FB}}}, \qquad (2)$$

where $\boldsymbol{r}_i(t_j)$ is the position of the ith particle at the jth frame (discrete time t_j). N_{I}, N_{Fi}, and Δt_{frm} indicate the number of individual particles (trajectories), the number of frames in the ith trajectory, and the time span to evaluate the trajectories, i.e., $\Delta t_{\mathrm{frm}} = t_{j+1} - t_j$, respectively. $D_{\mathrm{FB}\alpha}$ and α_{FB} are the numerically evaluated values of D_{α} and α through the frame-based (FB) averaging [33]. $D_{\mathrm{FB}\alpha}$ and α_{FB} are obtained by the least-squares fitting.

TABLE II. Input parameters for the PIV analysis consisting of three steps [43,44].

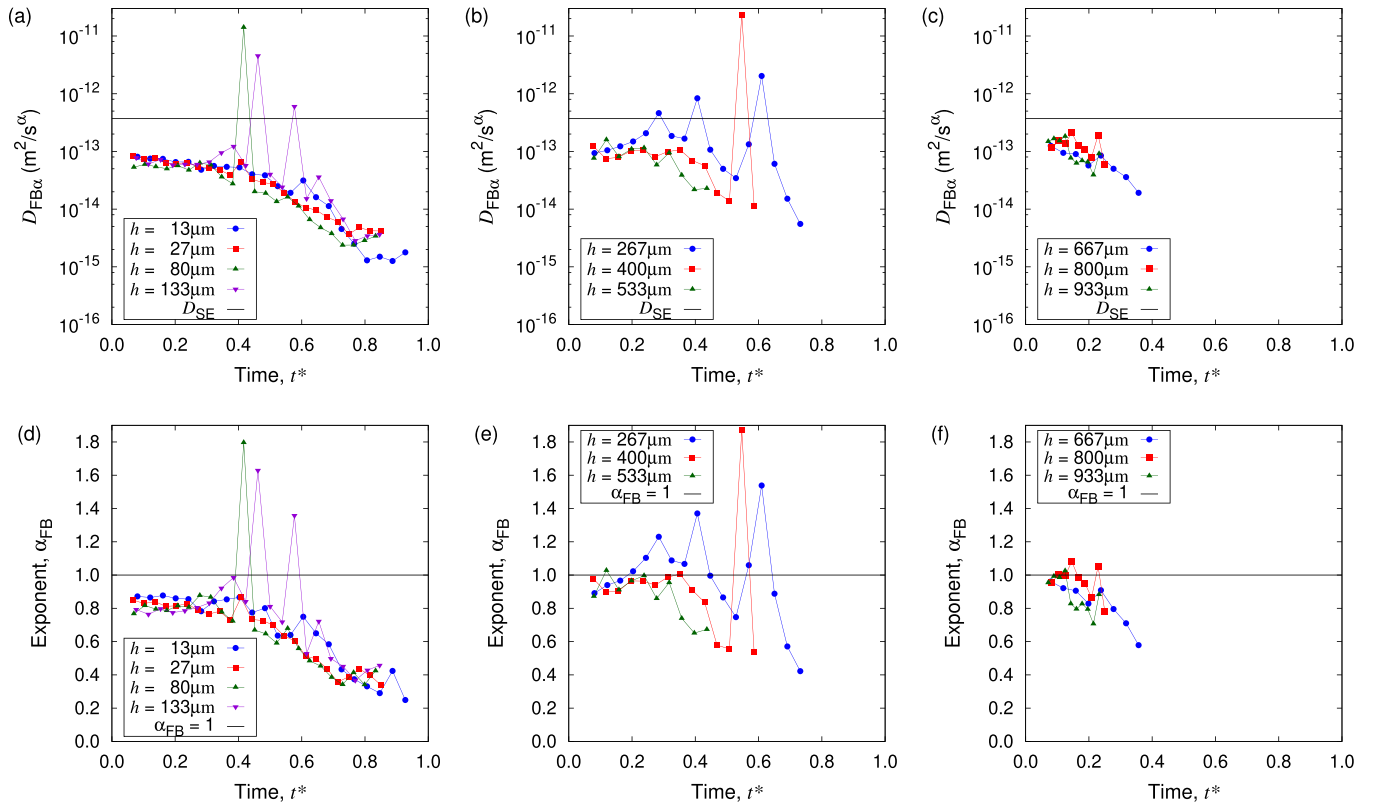|	Parameter	Value
PIV1	Interrogation size (px)	128
	Search size (px)	256
	Vector space (px)	64
PIV2	Interrogation size (px)	96
	Search size (px)	192
	Vector space (px)	48
PIV3	Interrogation size (px)	64
	Search size (px)	128
	Vector space (px)	32
	Correlation threshold	0.6

FIG. 5. Time evolution of generalized diffusion coefficient $D_{FB\alpha}$ [(a)–(c)] and its scaling exponent α_{FB} [(d)–(f)] at horizontal center of the container with different observation heights h. Dimensionless time t^* is defined so that $t^* = 1$ corresponds to the macroscopic drying up time.
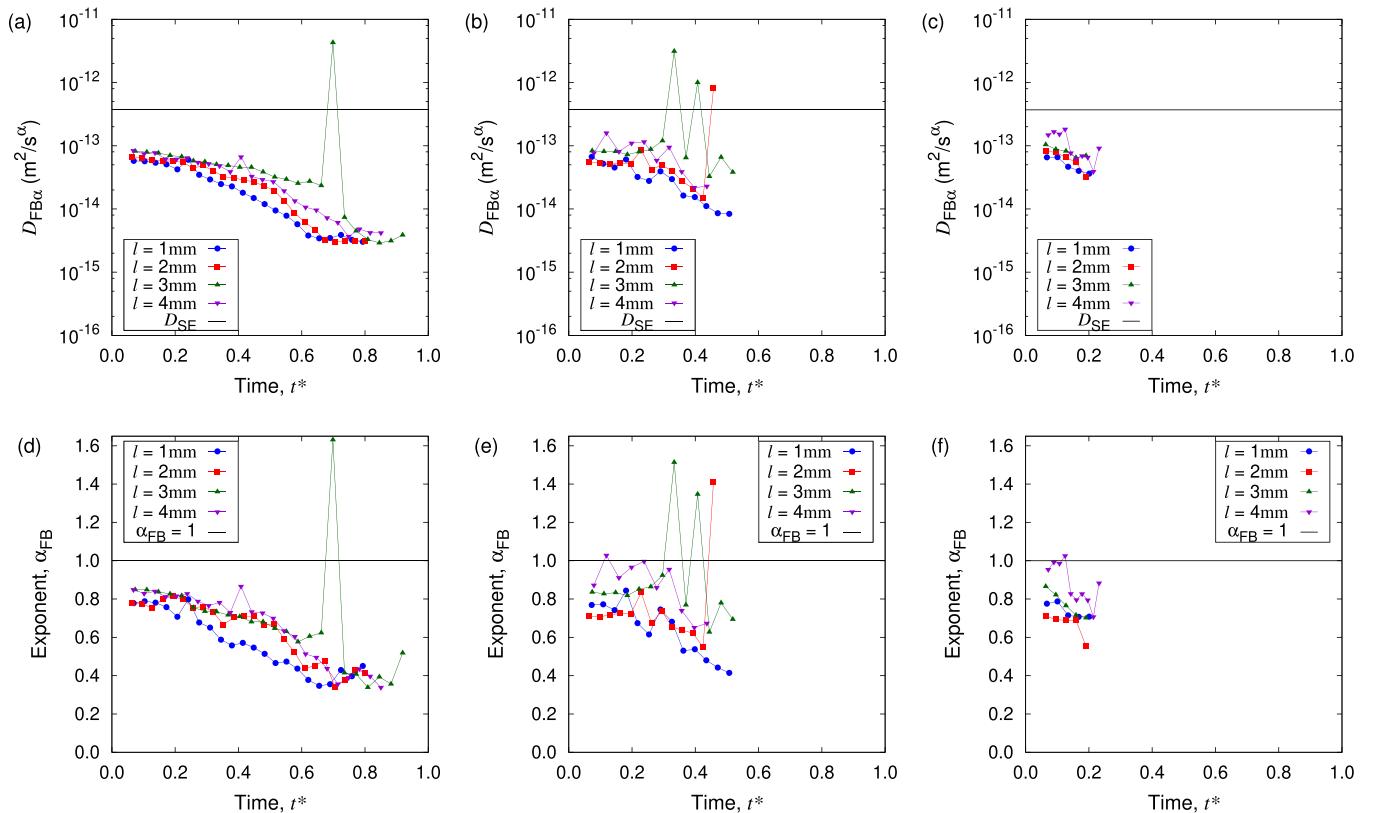

FIG. 6. Time evolution of generalized diffusion coefficient $D_{FB\alpha}$ [(a)–(c)] and its scaling exponent α_{FB} [(d)–(f)] for different distances l from the sidewall at heights h of (a) and (d) 27 μm, (b) and (e) 533 μm, and (c) and (f) 933 μm, respectively. Dimensionless time t^* is defined so that $t^* = 1$ corresponds to the macroscopic drying up time.
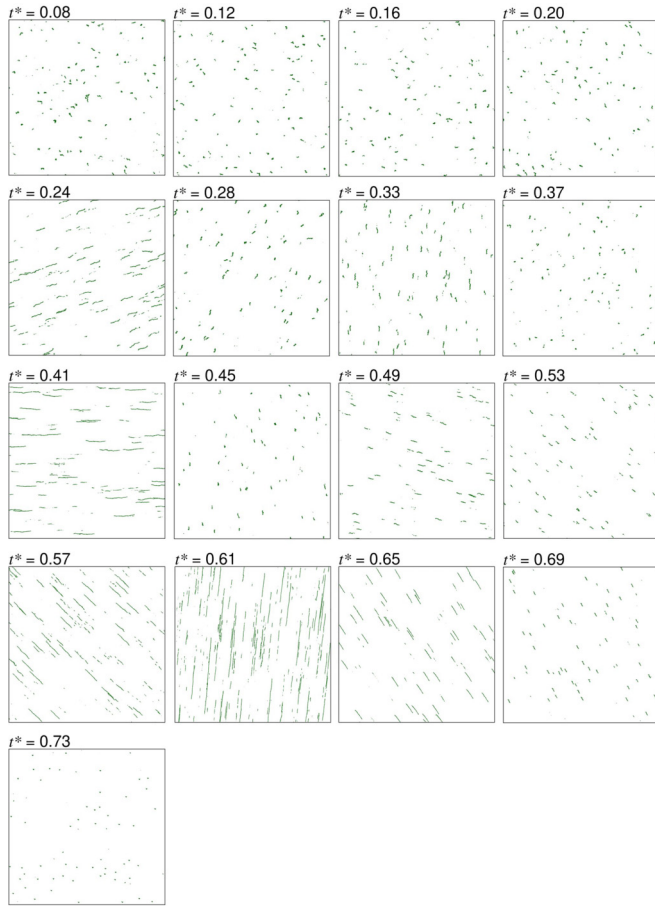
FIG. 7. Trajectories in single movie data of 10 s at the horizontal center ($l = 4$ mm) and $h = 267$ μm corresponding to the data in Figs. 5(b) and 5(e). Each subfigure corresponds to a square with 166.4 μm on a side.

2. PIV and evaluation of velocity field characteristics

We conducted the PIV analysis based on the normalized cross correlation [43] for the time-series images obtained from the digital camera. Each image was first trimmed to have squares of circumscription to the circular disk of sample domain for computational efficiency. The irrelevant subdomain outside the circular sample domain was defined as null to prevent the obvious noise. The colors were gray scaled and each time-sequential pair of images was analyzed. The PIV analysis employed here is based on the region of interest (ROI) instead of particle tracking in contrast to the above-mentioned SPT analysis for the microscopy images. Nevertheless, the spatial variation of the light intensity due to the existence of probe particles are useful for the cross-correlation analysis. The typical number of probe particles per 1 px^2 are estimated to be 14 to 15 for $6.3 - 6.5$ μm/px. The slight fluctuation of length per pixel originates from the focusing of the camera for each experiment.

The necessary input parameters for the PIV analysis are summarized in Table II. The interrogation window (IW) corresponds to the ROI, and the search window (SW) size defines the range of search to evaluate the cross correlation. The vector spacing (VS) indicates the distance between the centers

of ROI. The algorithm [43] employed in this paper proceeds as three steps of the similar process, which was executed by the ImageJ plug in [44]. Specific parameters were decided based on the IW size 64 px of PIV3 (the third step of the iterative analysis). For example, the SW size is twice that of the IW size, and VS is a half of the IW size. The numerical values of parameters in PIV1 and PIV2 are 200% and 150% of those in PIV3.

A single set of PIV analysis (consisting of three steps) yields a single map of velocity field. The time-series images allows time-series evaluation of consecutive pair of images. Although we will also show some typical velocity maps in the next section, the number of such maps to be explicitly observed are limited. Therefore, we also represent the basic characteristics of velocity fields by three quantities to read the time evolution in the whole range of drying process. Besides the mean and standard deviations of the velocity field to represent the basic criteria of space distribution, we also evaluate the velocity autocorrelation function (VACF) in terms of distance as follows:

$$\text{VACF}(r) = \frac{\langle \boldsymbol{v}(r) \cdot \boldsymbol{v}(0) \rangle}{\langle \boldsymbol{v}(0) \cdot \boldsymbol{v}(0) \rangle}, \qquad (3)$$

where $\boldsymbol{v}(r)$ is the evaluated velocity vector at distance r from the arbitrary reference position to be used for the evaluation of another velocity vector within the sample domain. Since VACF(r) is a function of r, we define a characteristic correlation length $\lambda_{\text{VACF} \approx 0.1}$ by the distance at which VACF decays below 0.1 [i.e., 10% of VACF(0)]. Although the value 0.1 does not indicate special meaning here, this is defined so that the VACF substantially decays, and still it is beyond 0. Thereby the huge fluctuation of correlation length as a function of time is prevented.

III. RESULTS AND DISCUSSION

We first discuss the microscopic dynamics of Brownian probe particles in the aqueous CNF dispersion in the container with the PTFE sidewall, focusing on the time evolution of rheological characteristics in the drying process. Figures 5 and 6 show the generalized diffusion coefficient $D_{\text{FB}\alpha}$ and its scaling exponent α_{FB} as a function of dimensionless time t^*. The dependence on height h from the bottom wall was examined at the horizontal center (Fig. 5), and that on the distance l from the sidewall was examined at different heights h (Fig. 6). The increase in CNF concentration due to the drying process leads to the lower $D_{\text{FB}\alpha}$ and α_{FB}. The significant decrease in $D_{\text{FB}\alpha}$ and α_{FB} (i.e., slope of these quantities as a function of time) tend to occur earlier in the top domain of the sample compared in the bottom domain. This trend suggests the earlier network formation of CNFs in the domain sufficiently close to the air-liquid interface.

Besides these rheological characteristics, transient drastic increase in $D_{\text{FB}\alpha}$ and α_{FB} are observed in the middle stage of drying process $t^* \approx 0.4$–0.7. These transient rises are attributed to the persistent motion or flow since $\alpha_{\text{FB}} > 1$. It is also supported by the spatial correlation of persistent displacements in the trajectory map visualized in Fig. 7. The direction of persistent displacement is different among the specific events. It should be noted that small portion of the
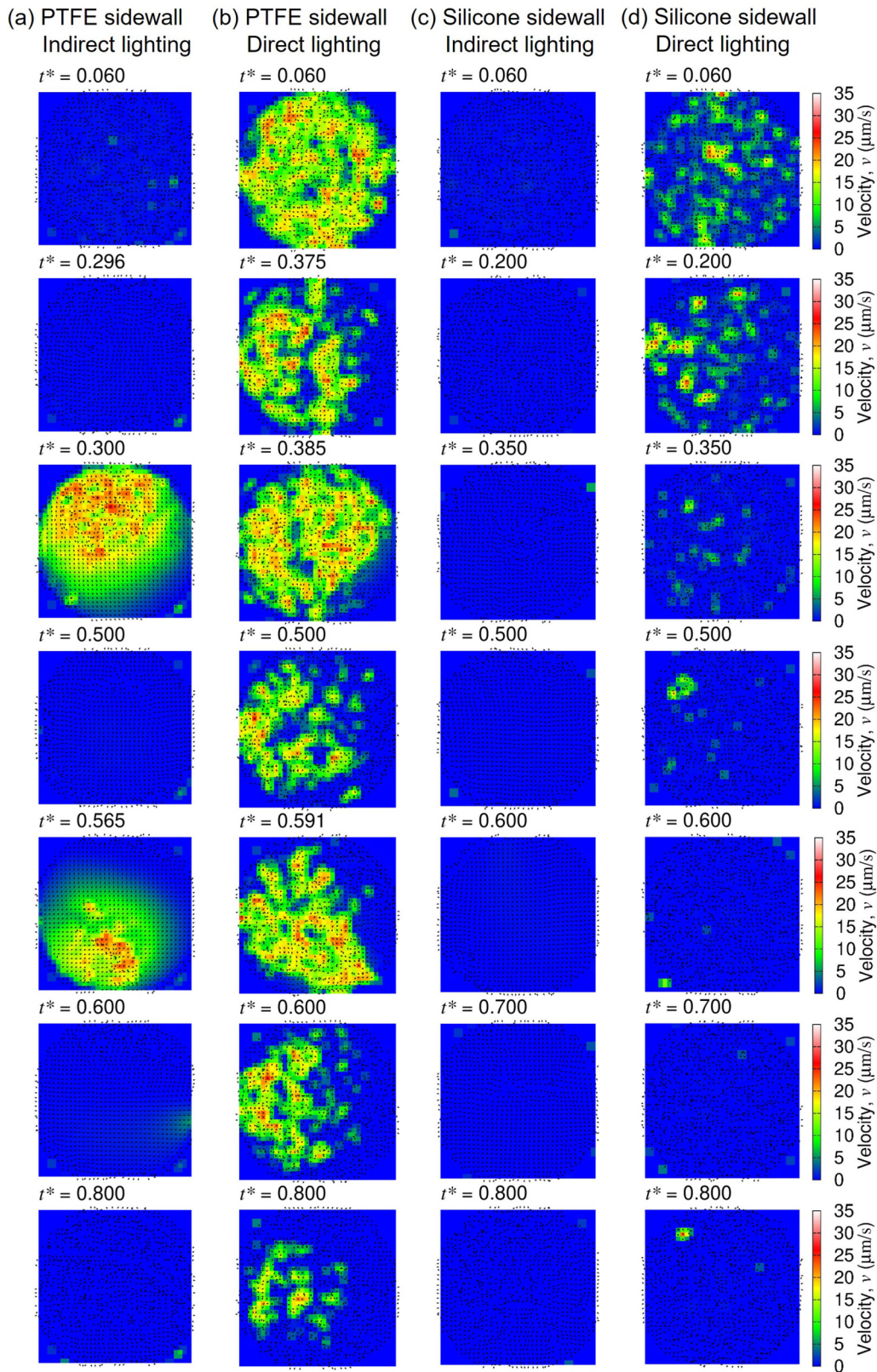
FIG. 8. Velocity field maps obtained from the PIV analysis in the time series for different sidewall and lighting conditions. The sidewall conditions are schematically shown in Fig. 1. Indirect lighting and direct lighting conditions correspond to Figs. 3(a) and 3(b), respectively. Dimensionless time t^* is defined so that $t^* = 1$ corresponds to the macroscopic drying up time.
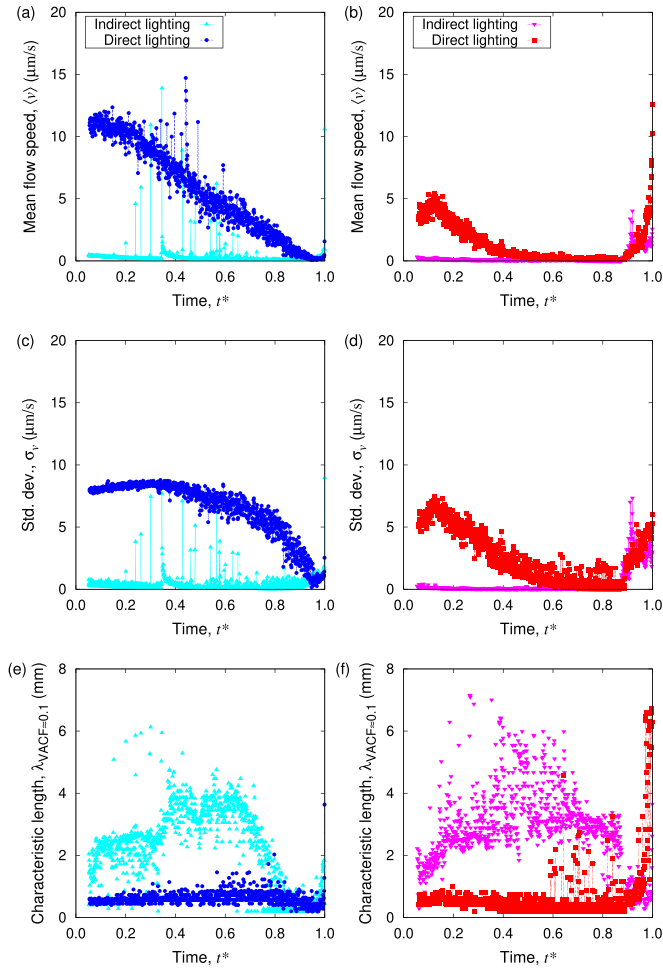
FIG. 9. Time evolution of the mean [(a) and (b)] and standard deviation [(c) and (d)] of the velocity fields and characteristic correlation length $\lambda_{VACF \approx 0.1}$ [(e) and (f)] for the cases with PTFE [(a), (c), and (e)] and silicone [(b), (d), and (f)] sidewalls, respectively. Indirect lighting and direct lighting conditions correspond to Figs. 3(a) and 3(b), respectively. Dimensionless time t^* is defined so that $t^* = 1$ corresponds to the macroscopic drying up time.

CNF is sufficient to suppress the coffee-ring phenomenon [35,36]. Sufficient suppression of the coffee-ring effect should be valid to Marangoni convection as well. The late stage
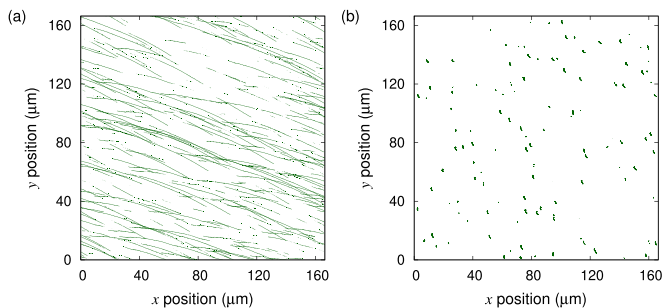

FIG. 10. Trajectories in single movie data of 10 s at the horizontal center ($l = 4$ mm) and $h = 400$ μm when (a) $t^* = 0.55$ and (b) $t^* = 0.51$ corresponding to the data in Figs. 5(b) and 5(e).

($t^* > 0.7$) of the drying process show substantially lower α_{FB} than the middle stage, which indicates the gelation.

The transient flow in the middle stage of drying is not necessarily a single event. In fact, its multiple occurrence is observed in Figs. 5 and 6. Furthermore, the space scale captured by the SPT was 166.4×166.4 μm^2, and a single movie duration was 10 s with an interval of 300 s due to the huge amount of data. Therefore, we examine the global nature of this flow by the PIV analysis where the space scale captures the entire sample of 8-mm disk in the horizontal directions and the flow field is evaluated at every interval of 10 s. The typical flow fields are shown in the time series in Fig. 8, and the time evolution of characteristic quantities obtained from the PIV analysis are shown as a full time series in Fig. 9. The difference in rheological time evolution at the surface and the rest of the system calls for the possible distinction. Therefore, the space resolution in the vertical direction is covered by the different lighting condition. The indirect lighting condition focuses on the characteristics near the air-liquid interface, whereas the the direct lighting condition simply captures the entire sample through the vertically transmitted light (cf. Figs. 3 and 4). We also found that the persistent displacement field is not completely uniform but includes significant variation of direction within the focal depth of the inverted optical microscope depending on the observation position, which is confirmed from the crossing of smooth trajectories as shown in Fig. 10.

The indirect lighting condition [cf. Fig. 8(a)] clearly shows the sudden transient flow field (e.g., at $t^* = 0.300$ and 0.565). The flow field is not symmetric despite the circular shape of the container bottom wall. Furthermore, the subdomain of highest flow speed does not show fully concerted flow direction but rather randomly distributed. In contrast, the direct lighting condition [Fig. 8(b)] shows the overall velocity field that is rather randomly distributed in the direction and its gradual and rather monotonic decrease in the speed. This characteristic corresponds to the CNF network formation that
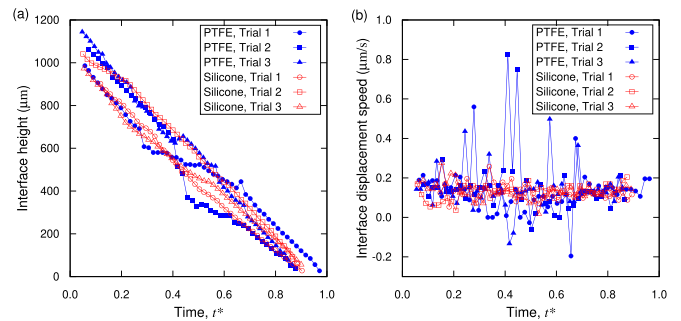

FIG. 11. Time evolution of the air-liquid interface at $l = 1$ mm in the cases of the PTFE and silicone sidewalls. The positive speed of displacement is defined as the direction corresponding to the decreasing sample height. The interface was determined at 2.5-min intervals by the focal point of observation with the inverted optical microscope. The values of speed has the limitation of time resolution by this interval. The trials of these drying experiments in this figure are independent from the rest of the measurements of other figures whereas the sample conditions including the containers are consistent with them.

hinders the probe particle diffusion (cf. Figs. 5 and 6). It is also consistent with the variation of the flow direction at the same horizontal direction with the progress of drying process (cf. Fig. 7) These qualitative differences in the time evolution of the flow velocity field between the indirect and the direct lighting conditions may correspond to the faster drying process near the air-liquid interface observed in the SPT through the faster decrease in α_{FB}.

Since the location of maximum velocity appears to deviate from the center of the container, displacement of the air-liquid-solid interface line on the sidewall is likely to contribute to this intermittent flow. Therefore, we compare with the PIV map based on the drying process with the silicone sidewall of the container. The substantial difference is observed as shown in Figs. 8(c) and 8(d). The silicone sidewall resulted in the much lower flow speed compared to the case of the PTFE sidewall. Furthermore, the intermittent flow was not observed in the case of the silicone sidewall. This difference in sidewall, at least, partly explains the absence of this level of drastic intermittent flow in our previous study [30] where some other conditions were also different. The difference in sidewall materials causes the difference in the time evolution of macroscopic air-liquid interface heights as shown in Fig. 11. In particular, the PTFE sidewall leads to the more drastic intermittent stick-slip motion compared to the silicone sidewall. This difference in the macroscopic sample dynamics in the vertical direction is considered to couple with the dynamics in the horizontal directions. Although the time resolution of Fig. 11 is limited to 2.5 min, Fig. 9 indicates that the main and typical motion of this intermittent dynamics takes place within the timescale of 10 s.

Although the velocity map shows rich information, Fig. 8 is only part of the whole time-series data. Therefore, we focus on the full time series of representative quantities obtained from the PIV analysis. Figures 9(a), 9(c) and 9(e) show the time evolution of mean value $\langle v \rangle$ and standard deviation σ_v of flow speed, and characteristic length $\lambda_{VACF\approx0.1}$ [Eq. (3)]

in the case of the PTFE sidewall. Figures 9(b), 9(d) and 9(f) show those in the case of silicone sidewall, respectively. Figures 9(a) and 9(b) show that the sudden drastic transient flow appears intermittently for many times in the middle stage of the drying process when the sidewall is the PTFE, whereas such drastic transient flow is absent when the sidewall is silicone. This feature is revealed by the indirect lighting condition. Figure 9(c) shows that the intermittent flow is also highly nonuniform. Nevertheless, Fig. 9(e) shows that the characteristic correlation length $\lambda_{VACF\approx0.1}$ of the intermittent flow is longer than the random flow field in the early stage of the drying process. In other words, random flow field in the early stage has comparable or higher mean and standard deviations of the speed, but the intermittent flow is more concerted dynamics.

Furthermore, $\lambda_{VACF\approx0.1}$ evaluated from indirect lighting shows the distinction of early, middle, and late stages of the drying process. Whereas the early stage shows significant correlation length, it is almost negligible in the late stage after the most concerted dynamics in the middle stage. This makes contrast with the random flow manifested by the direct lighting shows the monotonic decrease in mean and standard deviations of the speed, and the correlation length does not show significant transition of the drying stage. Roughly monotonic decrease in mean flow speed is confirmed in the direct lighting of both types of sidewall materials [cf. Figs. 9(a) and 9(b)]. The monotonically decreasing random velocity field is nonuniform, regardless of the sidewall materials. The significant increase in the speed at the final stage of drying, $t^* \approx 1$, observed in Fig. 9 corresponds to the peeling off of the nanopaper as shown in Fig. 12. The different wettability of the sidewall leads to the difference in the starting time of apparent film formation based on visual inspection of the sample, which typically begins at $t^* = 0.6$–0.7 and $t^* = 0.8$–0.9 for the cases of sidewalls of the PTFE and silicone, respectively. These time points also roughly correspond to the start of the late stage of drying in Fig. 9.
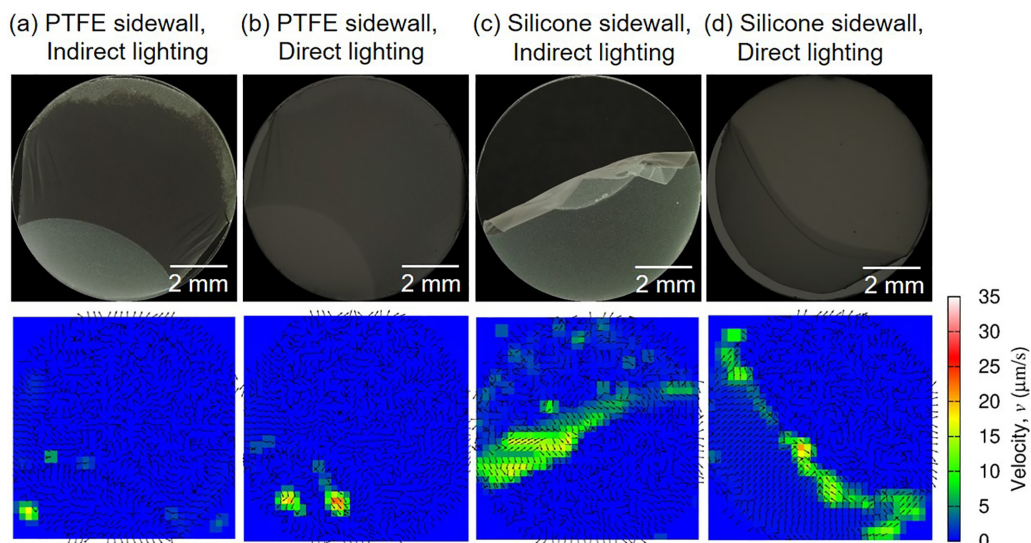

FIG. 12. Digital camera images of the peeling off of the nanopaper sample from the bottom wall and the corresponding velocity map at the final stage of drying ($t^* = 0.94$). Indirect lighting and direct lighting conditions correspond to Figs. 3(a) and 3(b), respectively. Dimensionless time t^* is defined so that $t^* = 1$ corresponds to the macroscopic drying up time.

IV. CONCLUSIONS

Since a small portion of CNFs suppresses the coffee-ring phenomenon, it has not been clear whether any significant flow can take place in a typical drying process in containers. We have revealed the precursory flow of CNF dispersion in the transient state of nanopaper formation. The nature of the precursory flow is subject to the boundary conditions assigned by the container used for drying the sample liquid.

The SPT ensures that the intermittent flow occurs in the intermediate state of rheological state transition for the cases of the PTFE sidewall. The PIV captures the nonuniform flow pattern in space. Furthermore, the PIV analysis of the entire period of the drying process reveals the frequent occurrence of this intermittent flow within the middle stage of the drying process. Consequently, three stages of the drying process are characterized: (1) early stage with random flow pattern without intermittent flow, (2) middle stage where intermittent flow is manifested, and (3) late stage without significant flow.

The occurrence of drastic intermittent flow depends on the surface property of the container sidewall, and it was not significant for the cases of the silicone sidewall. Nevertheless, the three stages of the drying process are characterized especially by the correlation length $\lambda_{\text{VACF}\approx0.1}$ defined in terms of the VACF. Although the mean and standard deviations of the flow speed exhibit roughly monotonic decreases in time for the silicone sidewall in contrast to the PTFE one, the space correlation of the flow velocity is high at the middle stage of the drying compared to the early and late stages. The middle stage of drying is the gelation process characterized by the long $\lambda_{\text{VACF}\approx0.1}$.

Thus, the relatively robust nature of $\lambda_{\text{VACF}\approx0.1}$ is attributed to the rheology of the aqueous CNF dispersion, whereas the nature of flow is substantially varied by the sidewall materials. The physical properties of the CNF films are determined by the drying process of aqueous CNF dispersion. Therefore, this paper provides the important information to the step forward for the fabrication process design of nanopapers and thin-film fabrication from gelating materials, in general.

[1] I. Gonzalez, M. Alcala, G. Chinga-Carrasco, F. Vilaseca, S. Boufi, and P. Mutje, From paper to nanopaper: Evolution of mechanical and physical properties, Cellulose **21**, 2599 (2014).

[2] A. Barhoum, P. Samyn, T. Ohlund, and A. Dufresne, Review of recent research on flexible multifunctional nanopapers, Nanoscale **9**, 15181 (2017).

[3] A. J. Benitez and A. Walther, Cellulose nanofibril nanopapers and bioinspired nanocomposistes: A review to understand the mechanical perpery space, J. Mater. Chem. A **5**, 16003 (2017).

[4] Q. Wang, Q. Yao, J. Liu, J. Sun, Q. Zhu, and H. Chen, Processing nanocellulose to bulk materials: A review, Cellulose **26**, 7585 (2019).

[5] F. Hoeng, A. Denneulin, and J. Bras, Use of nanocellulose in printed electronics: A review, Nanoscale **8**, 13131 (2016).

[6] C. Liao, M. Zhang, M. Y. Yao, T. Hua, L. Li, and F. Yan, Flexible organic electronics in biology: Materials and devices, Adv. Mater. **27**, 7493 (2015).

[7] O. Nechyporchuk, M. N. Belgacem, and J. Bras, Production of cellulose nanofibers: A review of recent advances, Ind. Crop. Prod. **93**, 2 (2016).

[8] H. Zhu, Z. Fang, C. Preston, Y. Li, and L. Hu, Transparent paper: Fabrications, properties, and device applications, Energy Environ. Sci. **7**, 269 (2014).

[9] M. Henriksson, L. A. Berglund, P. Isaksson, T. Lindstrom, and T. Nishino, Cellulose nanopaper structures of high toughness, Biomacromolecules **9**, 1579 (2008).

[10] A. Kulachenko, T. Denoyelle, S. Galland, and S. B. Lindstrom, Elastic properties of cellulose nanopaper, Cellulose **19**, 793 (2012).

[11] H. Zhu, S. Zhu, Z. Jia, S. Parvinian, Y. Li, O. Vaaland, L. Hu, and T. Li, Anomalous scaling law of strength and toughness of cellulose nanopaper, Proc. Natl. Acad. Sci. USA **112**, 8971 (2015).

[12] R. Mao, S. Goutianos, W. Tu, N. meng, S. Chen, and T. Peijs, Modeling the elastic properties of cellulose nanopaper, Mater. Des. **126**, 183 (2017).

[13] X. Qin, S. Feng, Z. Meng, and S. Keten, Optimizing the mechanical properties of cellulose nanopaper through surface energy and critical length scale considerations, Cellulose **24**, 3289 (2017).

[14] G. Molnar, D. Rodney, F. Martoia, P. J. J. Dumont, Y. Nishiyama, K. Mazeau, and L. Orgeas, Cellulose crystals plastify by localized shear, Proc. Natl. Acad. Sci. USA **115**, 7260 (2018).

[15] P. N. Ciesielski, R. Wagner, V. S. Bharadwaj, J. Killgore, A. Mittal, G. T. Beckham, S. R. Decker, M. E. Himmel, and M. F. Crowley, Nanomechanics of cellulose deformation reveal molecular defects that facilitate natural deconstruction, Proc. Natl. Acad. Sci. USA **116**, 9825 (2019).

[16] Q. Meng and T. J. Wang, Mechanics of strong and tough cellulose nanopaper, Appl. Mech. Rev. **71**, 040801 (2019).

[17] L. M. Mariani, W. R. Johnson, III, J. M. Considine, and K. T. Turner, Printing and mechanical characterization of cellulose nanofibril materials, Cellulose **26**, 2639 (2019).

[18] Q. Guan, H. Yang, Z. Han, L. Zhou, Y. Zhu, Z. Ling, H. Jiang, P. Wang, T. Ma, H. Wu, and S. Yu, Lightweight, tough, and sustainable cellulose nanofiber-derived bulk structural materials with low thermal expansion coefficient, Sci. Adv. **6**, eaaz1114 (2020).

[19] S. Ohira, D. Mizumura, and I. Hanasaki, Inkjet drawing dynamics of conductive polymer droplets on cellulose nanopapers, AIP Adv. **10**, 045122 (2020).

[20] C. Li, T. Kasuga, K. Uetani, H. Koga, and M. Nogi, High-speed fabrication of clear transparent cellulose nanopaper by applying humidity-controlled multi-stage drying method, Nanomaterials **10**, 2194 (2020).

[21] T. Tamiya, R. Soni, Y. Hsu, and H. Uyama, Highly water-tolerant TEMPO-oxidized cellulose nanofiber films using a maleic anhydride/wax copolymer, ACS Appl. Polym. Mater. **3**, 4625 (2021).

[22] A. Operamolla, S. Casalini, D. Console, L. Capodieci, F. D. Benedetto, G. V. Bianco, and F. Babudri, Tailoring water stability of cellulose nanopaper by surface functionalization, Soft Matter **14**, 7390 (2018).

[23] S. Chen, Y. Song, and F. Xu, Highly transparent and hazy cellulose nanopaper simultaneously with a self-cleaning superhydrophobic surface, ACS Sustainable Chem. Eng. **6**, 5173 (2018).

[24] C. Reverdy, N. Belgacem, M. S. Moghaddam, M. Sundin, A. Swerin, and J. Bras, One-step superhydrophobic coating using hydrohobized cellulose nanofibrils, Colloids Surf., A **544**, 152 (2018).

[25] R. Murase, S. Kondo, T. Kitamura, Y. Goi, M. Hashimoto, and Y. Teramoto, Cellulose nanofibers as a module for paper-based microfluidic analytical devices: Labile substance storage, processability, and reaction field provision and control, ACS Appl. Bio Mater. **1**, 480 (2018).

[26] K. Solin, H. Orelma, M. Borghei, M. Vuoriluoto, R. Koivunen, and O. J. Rojas, Two-dimensional antifouling fluidic channels on nanopapers for biosensing, Biomacromolecules **20**, 1036 (2019).

[27] H. Sehaqui, A. Liu, Q. Zhou, and L. A. Berglund, Fast preparation procedure for large, flat cellulose and cellulose/inorganic nanopaper structures, Biomacromolecules **11**, 2195 (2010).

[28] Y. Peng, D. J. Gardner, and Y. Han, Drying cellulose nanofibrils: In search of a suitable method, Cellulose **19**, 91 (2012).

[29] D. Mizumura, I. Hanasaki, Y. Ooi, and Y. Horikawa, Improving the macroscopic uniformity of nanopaper by multi-step coating of cellulose nanofibre dispersion, Micro Nano Lett. **12**, 516 (2017).

[30] T. Koitabashi and I. Hanasaki, Drying path dependence in microrheological characteristics of cellulose nanofiber dispersion revealed by single particle tracking, J. Phys. D: Appl. Phys. **54**, 295302 (2021).

[31] R. Tanaka, T. Saito, D. Ishii, and A. Isogai, Determination of nanocellulose fibril length by shear viscosity measurement, Cellulose **21**, 1581 (2014).

[32] R. Tanaka, T. Saito, H. Hondo, and A. Isogai, Influence of flexibility and dimensions of nanocelluloses on the flow properties of their aqueous dispersions, Biomacromolecules **16**, 2127 (2015).

[33] R. Motohashi and I. Hanasaki, Characterization of aqueous cellulose nanofiber dispersions from microscopy movie data of Brownian particles by trajectory analysis, Nanoscale Adv. **1**, 421 (2019).

[34] Y. Shimizu and I. Hanasaki, Partial structural order of gel-forming material detected as multimodal subdiffusion by logarithmic measure, J. Phys.: Condens. Matter **33**, 455101 (2021).

[35] Y. Ooi, I. Hanasaki, D. Mizumura, and Y. Matsuda, Suppresing the coffee-ring effect of colloidal droplets by dispersed cellulose nanofibers, Sci. Technol. Adv. Mater. **18**, 316 (2017).

[36] N. Koyama and I. Hanasaki, Spatio-temporally controlled suppression of the coffee-ring phenomenon by cellulose nanofibers, Soft Matter **17**, 4826 (2021).

[37] T. Yasuda, N. Sakumichi, U.-I. Chung, and T. Sakai, Universal Equation of State Describes Osmotic Pressure throughout Gelation Process, Phys. Rev. Lett. **125**, 267801 (2020).

[38] I. Hanasaki, K. Okano, H. Y. Yoshikawa, and T. Sugiyama, Spatiotemporal dynamics of laser-induced molecular crystal precursors visualized by particle image diffusometry, J. Phys. Chem. Lett. **10**, 7452 (2019).

[39] R. Klages, G. Radons, and I. M. Sokolov, *Anomalous Transport: Foundations and Applications* (Wiley-VCH, Weinheim, 2008).

[40] B. A. Dalton, I. F. Sbalzarini, and I. Hanasaki, Fundamentals of the logarithmic measure for revealing multimodal diffusion, Biophys. J. **120**, 829 (2021).

[41] Y. Ooi, I. Hanasaki, D. Mizumura, and Y. Matsuda, Self-peeling-off in the drying of particulate films mixed with cellulose nanofibers, Micro Nano Lett. **12**, 511 (2017).

[42] I. F. Sbalzarini and P. Koumoutsakos, Feature point tracking and trajectory analysis for video imaging in cell biology, J. Struct. Biol. **151**, 182 (2005).

[43] Q. Tseng, E. Duchemin-Pelletier, A. Deshiere, M. Balland, H. Guillou, O. Filhol, and M. Théry, Spatial organization of the extracellular matrix regulates cell-cell junction positioning, Proc. Nat. Acad. Sci. USA **109**, 1506 (2012).

[44] ImageJ Plugin, https://sites.google.com/site/qingzongtseng/piv.

[45] K. Metzler and J. Klafter, The random walk's guide to anomalous diffusion: A fractional dynamics approach, Phys. Rep. **339**, 1 (2000).